Emergent Materials (2019) 2:487–494
https://doi.org/10.1007/s42247-019-00058-0

ORIGINAL ARTICLE

A phase transformation route to porous 2D Mn_3O_4 nanosheets with promising anode performance for Li-ion batteries

Nutpaphat Jarulertwathana[1] · Xiaoyan Jin[2] · Seong-Ju Hwang[2]

Received: 11 April 2019 / Accepted: 4 October 2019 / Published online: 28 October 2019

Abstract

A phase transformation route to porous 2D Mn_3O_4 nanosheets is developed by heat treatment of exfoliated layered MnO_2 nanosheets. The calcination of MnO_2 nanosheets at an elevated temperature of ≥ 500 °C in Ar atmosphere leads to the formation of porous 2D nanosheets as well as to reductive phase transition to low-valent Mn_3O_4. The formation of spinel-structured Mn_3O_4 phase with mixed tetrahedral and octahedral local symmetries is obviously evidenced by micro-Raman and X-ray absorption spectroscopies. An elevation of heating temperature enlarges the surface pore of 2D nanosheet and lowers the average oxidation state of Mn ion. In comparison with Mn_3O_4 crystal, the porous 2D Mn_3O_4 nanosheets show higher electrode activities for lithium ion batteries (LIBs) with larger discharge capacities, better rate characteristics, and excellent cyclabilities, emphasizing the advantage of porous 2D nanosheet morphology in optimizing the electrode functionality of metal oxide. The present study underscores the validity of the present phase transformation route in exploring novel high-performance metal oxide–based LIB electrode materials.

Keywords Phase transformation route · Porous 2D nanosheet · Mn_3O_4 · Electrode functionality · Lithium ion batteries

1 Introduction

Nanostructured manganese oxides have attracted research interest as promising electrode materials for lithium ion batteries (LIBs) because of their high electrochemical activity, economic and ecological merits, and rich abundance of the element Mn [1–4]. Depending on the oxidation state of Mn ions, manganese oxides are applicable both as cathode and as anode materials for LIBs [5–8]. While the intercalation mechanism is responsible for the cathode functionality of MnO_2 [9–12], the functionality of low-valent manganese oxides as anode materials relies on both the conversion and the alloying–dealloying mechanisms [2, 8, 13]. It is of prime importance that highly anisotropic two-dimensional (2D) manganese oxide nanosheet boasts many advantages such as the short Li diffusion path, the large surface area, and the large population of surface-active sites [14–16]. Although 2D nanosheets of layered MnO_2 can be prepared by soft-chemical exfoliation reaction or surfactant-assisted crystal growth [17, 18], it is fairly difficult to synthesize highly anisotropic 2D nanosheet of low-valent Mn_3O_4 phase because of its non-layered structure. Taking into account the fact that heat treatment would induce a phase transformation from MnO_2 to low-valent manganese oxides [19], exfoliated MnO_2 nanosheet can be employed as a precursor to 2D Mn_3O_4 nanosheet. The oxygen loss caused by the heat treatment at elevated temperature can cause the formation of porous 2D nanosheets [19]. The resulting porous 2D nanosheet morphology is highly advantageous in optimizing the electrode performance of metal oxide via the enhancement of ion-diffusion property [2, 4, 7, 20, 21]. Despite intense research efforts devoted for nanostructured low-valent manganese oxides [3, 7, 17, 22–24], we are unaware of any other report about the synthesis of porous 2D Mn_3O_4 nanosheet and its application as LIB electrode.

In this work, an efficient methodology to synthesize porous 2D Mn_3O_4 nanosheets is developed for the first time in terms of thermally induced phase transition of MnO_2 nanosheets.

Electronic supplementary material The online version of this article (https://doi.org/10.1007/s42247-019-00058-0) contains supplementary material, which is available to authorized users.

✉ Seong-Ju Hwang
hwangsju@yonsei.ac.kr

[1] Center for Hybrid Interfacial Chemical Structure (CICS), Department of Chemistry and Nanoscience, Ewha Womans University, Seoul 03760, Republic of Korea

[2] Center for Hybrid Interfacial Chemical Structure (CICS), Department of Materials Science and Engineering, Yonsei University, Seoul 03722, Republic of Korea

The evolutions of the crystal and electronic structures of precursor MnO_2 nanosheet upon the heat treatment are systematically investigated via X-ray diffraction, electron microscopic analysis, Raman microscopy, and X-ray absorption fine structure techniques. The resulting porous Mn_3O_4 nanosheets are tested as anode materials for LIBs to elucidate the effect of surface pore on the electrode functionality of metal oxide.

2 Experimental

Synthesis The precursor of 2D MnO_2 nanosheet was synthesized by soft-chemical solution-based synthesis, as reported previously [18]. To minimize the concentration of surfactant tetramethylammonium (TMA^+) ions in the resulting colloidal suspension, the as-prepared colloidal suspensions of MnO_2 were subjected to dialysis for 3 days. The exfoliated MnO_2 nanosheets were restored from this colloidal suspension by freeze-drying. The formation of low-valent manganese oxides was achieved by heat treatment of the restored MnO_2 nanosheets at 300–800 °C for 3 h with a heating rate of 100 °C h^{-1} in Ar atmosphere. The resulting calcined derivatives at 300–800 °C are denoted as **MnAr3**–**MnAr8**, respectively, where the trailing numbers indicate the heating temperature.

Material characterization The crystal structure of the present materials was characterized by powder X-ray diffraction (XRD, Rigaku D/Max-2000/PC, Ni-filtered Cu K_α radiation, λ = 1.5418 Å, 298 K) analysis. The morphological evolution of the precursor nanosheets upon the heat treatment was studied with transmission electron microscopy (TEM) using a Jeol JEM-2100F electron microscope and field emission-scanning electron microscopy (FE-SEM) using a Jeol JSM-6700F microscope equipped with an energy dispersive X-ray spectrometer (EDS). Micro-Raman spectroscopic analysis was carried out using a Horiba Jobin Yvon LabRam Aramis spectrometer, where the Ar ion laser with λ = 514.5 nm was utilized as an excitation source. The Mn K-edge X-ray absorption near-edge structure/extended X-ray absorption fine structure (XANES/EXAFS) spectra were collected at beam line 10C of the Pohang Accelerator Laboratory (PAL, Pohang, Korea). The energy calibration for the collected XANES/EXAFS spectra was achieved by simultaneously measuring the reference spectrum of Mn metal foil. The N_2 adsorption–desorption isotherms of the present materials were measured at 77 K using Micromeritics ASAP 2020 to probe their pore structures.

Electrochemical measurement The electrochemical cycling tests were carried out for the obtained porous nanosheets with a cell consisting of 1 M $LiPF_6$ in ethylene carbonate:diethyl carbonate (EC:DEC, 50:50 v/v) and 3 vol% fluoroethylene carbonate (FEC). The composite electrode was prepared by thoroughly mixing the active material (70wt%) with Super P (20wt%) and polyvinylidene fluoride (PVDF) (10wt%) in *N*-methyl-2-pyrrolidinone (NMP) solvent. All the charge–discharge tests were carried out in a galvanostatic mode with a Maccor (Series 4000) multichannel galvanostat/potentiostat in the voltage range of 0.01–3.0 V with several current densities. Electrochemical impedance spectroscopy (EIS) measurements were performed by employing an alternating current voltage of 5-mV amplitude in the frequency range of 100 kHz–0.01 Hz.

3 Results and discussion

Figure 1 plot (a) presents the powder XRD patterns of the precursor MnO_2 nanosheet and its derivatives calcined at 300–700 °C. The precursor MnO_2 nanosheets restored by freeze-drying process show a series of well-developed (*00l*) reflections at low-angle region, indicating the formation of TMA^+-intercalated phase with expanded basal spacing. The derivatives calcined at 400–600 °C (Fig. 1 plot (c–e)) commonly display distinct XRD peaks of crystalline Mn_3O_4 phase (JCPDS no. 89-4837), indicating the reductive phase transformation into lower-valent manganese oxide. An elevation of heating temperature to 700 °C (Fig. 1 plot (f)) leads to the phase transition to Mn_3O_4 and also to the formation of small amount of impurity phases such as Mn_2O_3 and λ-MnO_2. The elevation of heating temperature to 800 °C leads to the advent of weak impurity peaks corresponding to Mn_2O_3 and λ-MnO_2 phases (see Fig. S1(a)). The thermally induced phase transition from MnO_2 to Mn_3O_4 is cross-confirmed by micro-Raman spectroscopic analysis. As plotted in Fig. 2, distinct

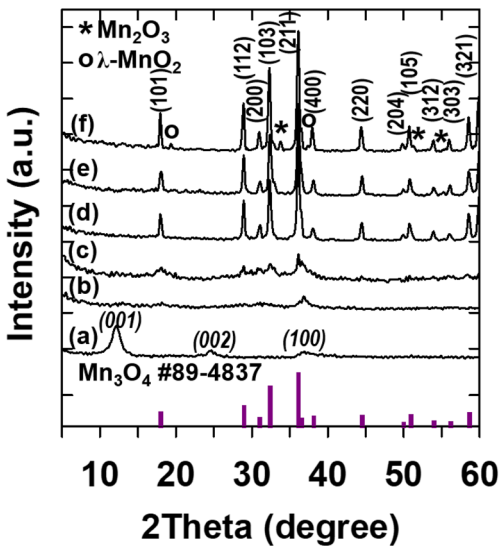

Fig. 1 Powder XRD patterns of (a) the precursor MnO_2 nanosheet and its calcined derivatives of (b) **MnAr3**, (c) **MnAr4**, (d) **MnAr5**, (e) **MnAr6**, and (f) **MnAr7**

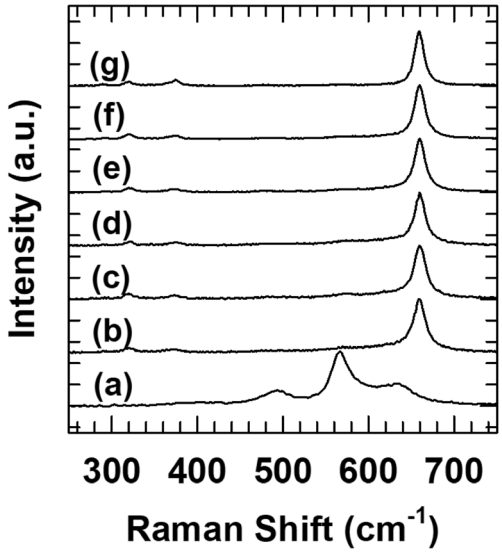

Fig. 2 Micro-Raman spectra of (a) the precursor MnO_2 nanosheet and its calcined derivatives of (b) **MnAr3**, (c) **MnAr4**, (d) **MnAr5**, (e) **MnAr6**, and (f) **MnAr7**, and (g) the reference Mn_3O_4

phonon lines of Mn_3O_4 phase [25] are discernible at 320, 375, and 660 cm^{-1} for all the calcined derivatives, which is in stark contrast to the spectral features of the precursor layered MnO_2 nanosheet (Fig. 2(a)) centering at 490, 565, and 635 cm^{-1} [19]. It is worthwhile to mention that, despite very diffuse and broad XRD patterns of **MnAr3**, this material also exhibits well-developed Raman features of Mn_3O_4 phase, confirming the occurrence of local structural transformation to Mn_3O_4 phase even at 300 °C.

The TEM images of the precursor MnO_2 nanosheet and its calcined derivatives are depicted in Fig. 3 and S2(a). The precursor MnO_2 nanosheet shows highly anisotropic 2D morphology with the lateral size of several micrometer. The EDS–elemental mapping analysis confirms the homogeneous distribution of Mn and O elements in the MnO_2 nanosheet (Fig. S3). As illustrated in Fig. 4, the FE-SEM images clearly demonstrate the maintenance of the 2D morphology of the precursor nanosheet upon the heat treatment at 300–700 °C. According to the FE-SEM and TEM results, the heat treatment at ≥ 500 °C causes the formation of highly porous 2D structure composed of porously aggregated nanocrystals. The present results clearly demonstrate the usefulness of the exfoliated MnO_2 nanosheet as a precursor for porous 2D nanostructured aggregates of low-valent manganese oxide nanocrystals.

The effects of heat treatment on the surface areas and pore structures of MnO_2 nanosheets are investigated with N_2 adsorption–desorption isotherm measurements, see Fig. 5 and Fig. S1(b). All the materials under investigation demonstrate the Brunauer–Deming–Deming–Teller (BDDT)-type IV shape of isotherm and H4-type hysteresis loop in the IUPAC classification, indicating the presence of the open slit-shaped capillaries with very wide bodies and narrow short necks [26]. The observation of distinct hysteresis at $pp_0^{-1} > 0.5$ strongly suggests that most of the porosity in the calcined derivatives is attributable to the formation of mesopores due to the restacking of 2D nanosheets [19]. The surface areas of the present materials are determined by the Brunauer–Emmett–Teller (BET) equation, as listed in Table S1. The surface areas of **MnAr3**–**MnAr6** are greater than that of MnO_2 nanosheets, indicating the enhancement of porosity after calcination at 300–600 °C. As the heating temperature increases to ≥ 700 °C, the surface areas of the calcined materials become smaller, which is attributable to the collapse of the stacking structure of 2D nanosheets. The formation of impurity Mn_2O_3 and MnO_2

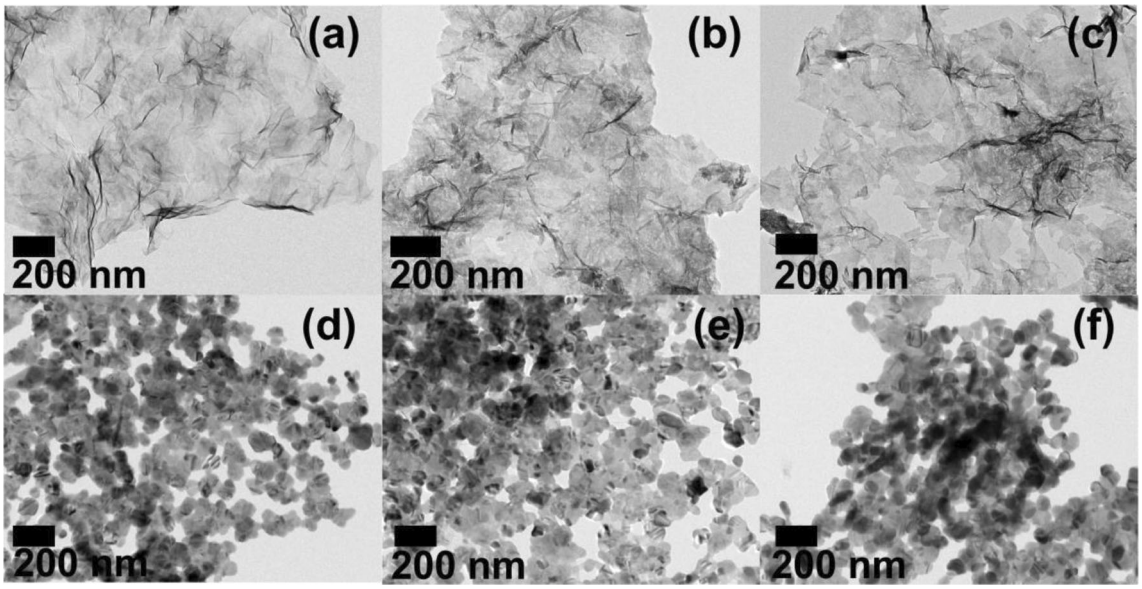

Fig. 3 TEM images of (a) the precursor MnO_2 nanosheet and its calcined derivatives of (b) **MnAr3**, (c) **MnAr4**, (d) **MnAr5**, (e) **MnAr6**, and (f) **MnAr7**

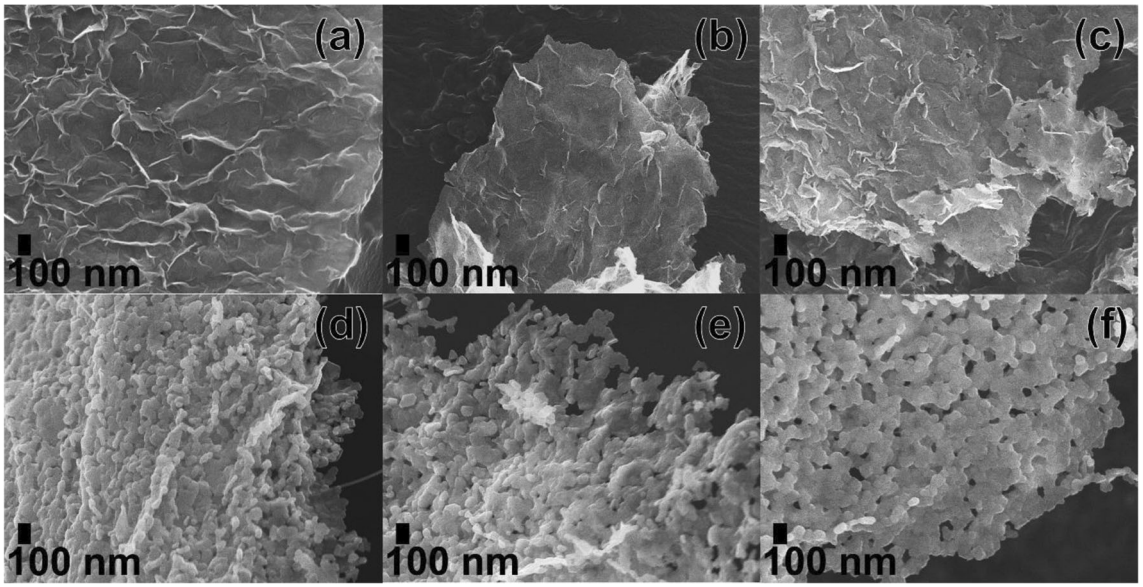

Fig. 4 FE-SEM images of (a) the precursor MnO_2 nanosheet and its calcined derivatives of (b) **MnAr3**, (c) **MnAr4**, (d) **MnAr5**, (e) **MnAr6**, and (f) **MnAr7**

phases can make additional contribution to the depressed surface areas of **MnAr7** and **MnAr8**. The pore volumes of the calcined derivatives show similar temperature dependence to the corresponding surface areas, reflecting the crucial contribution of pore volume to the expanded surface area of calcined derivative (Table S1).

To examine the effect of heat treatment on the electronic structure and local atomic arrangement of the precursor MnO_2 nanosheet, Mn K-edge XANES spectra of the present materials are investigated. The Mn K-edge XANES spectra of the precursor MnO_2 nanosheet and its calcined derivatives are plotted in Fig. 6A, along with the reference Mn_3O_4 crystal. The heat treatment at elevated temperature induces a gradual red-shift of main-edge position with the increase in the heating temperature, indicating the lowering of the Mn oxidation state of the precursor MnO_2 (the right panel of Fig. 6A). As can be seen clearly from Fig. 6B, the precursor MnO_2 nanosheet exhibits weak intensity for the pre-edge P and P' peaks corresponding to the dipole-forbidden 1s → 3d transitions, indicating the octahedral symmetry of manganese ions [27–29]. In comparison with the precursor MnO_2, all the calcined derivatives display a stronger pre-edge peak P at a lower energy, like the reference spectrum of spinel-structured Mn_3O_4. The enhancement of pre-edge peak upon the heat treatment strongly suggests the formation of MnO_4 tetrahedra in the calcined derivatives [27]. This result confirms the formation of spinel-structured Mn_3O_4 phase with mixed tetrahedral and octahedral local symmetries upon the heat treatment. The reductive-phase transformation to Mn_3O_4 is further confirmed by the variation of main-edge spectral features related to dipole-allowed 1s → 4p transitions [27–29]. All the calcined derivatives commonly exhibit similar main-edge spectral features to those of the reference Mn_3O_4, verifying the phase transformation into Mn_3O_4 structure. The present XANES results are in good agreement with the powder XRD and micro-Raman results (Figs. 1 and 2). The local structural change of Mn ion upon the heat treatment is cross-confirmed by Mn K-edge EXAFS analysis. As presented in Fig. 7A, all the calcined materials display similar k^3-weighted EXAFS oscillations to that of the reference Mn_3O_4. Similarly, all the calcined materials commonly show the Fourier-

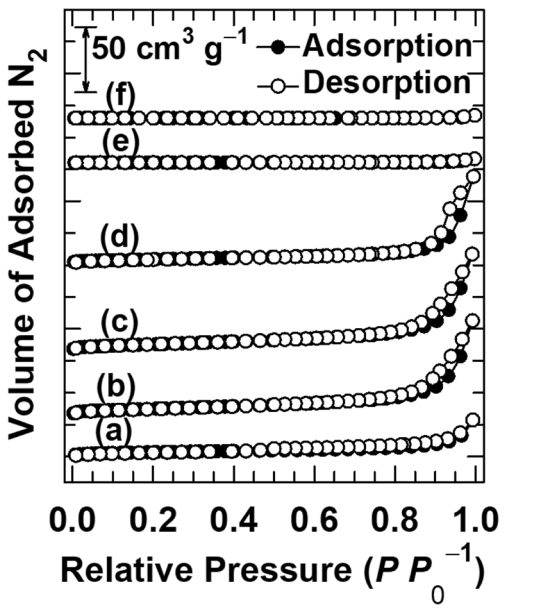

Fig. 5 N_2 adsorption–desorption isotherms of (a) the precursor MnO_2 nanosheet and its calcined derivatives of (b) **MnAr3**, (c) **MnAr4**, (d) **MnAr5**, (e) **MnAr6**, and (f) **MnAr7**

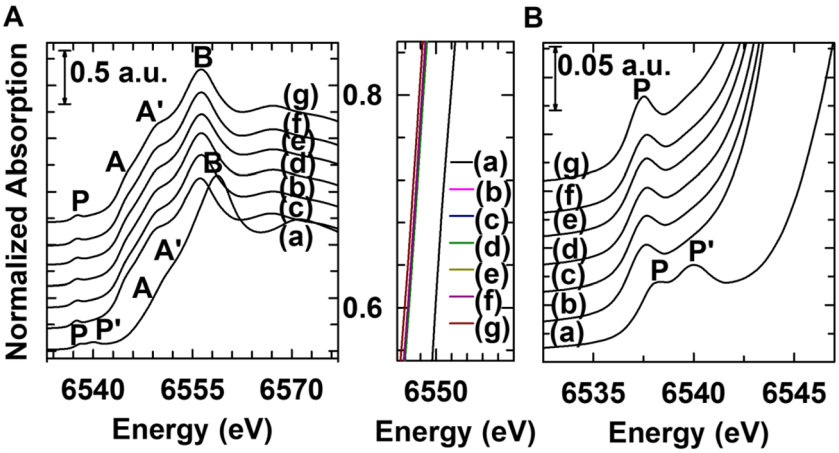

Fig. 6 (A) Mn K-edge XANES spectra and (B) their expanded view for pre-edge region of (a) the precursor MnO_2 nanosheet and its calcined derivatives of (b) **MnAr3**, (c) **MnAr4**, (d) **MnAr5**, (e) **MnAr6**, and (f) **MnAr7**, and (g) the reference Mn_3O_4

transformed (FT) peaks at ~ 1.5, ~ 2.4, ~ 2.9, and ~ 3.2 Å, which are assigned as (Mn–O), $(Mn–Mn)_{edge\text{-}shared}$, (Mn–Mn), and $(Mn–Mn)_{corner\text{-}shared}$ coordination shells, respectively (Fig. 7B) [30–32]. This spectral feature is typical of Mn_3O_4 structure but distinguishable from that of the precursor MnO_2 nanosheet, confirming the phase transition to Mn_3O_4. The elevation of heating temperature results in the enhancement of FT peak intensity, reflecting the enhancement of the crystallinity of Mn_3O_4 phase (the right panel of Fig. 7B).

The LIB electrode performances of the porous 2D Mn_3O_4 nanosheets as well as the reference Mn_3O_4 crystal are studied by measuring galvanostatic discharge–charge cycling data to probe the effect of porous nanosheet morphology on the electrode performance of manganese oxide. The LIB performances of the present materials are measured at a current density of 100 mA g^{-1} between 0.01 and 3.0 V vs. Li^+/Li for the 1st, 2nd, 10th, and 50th cycles, respectively. As plotted in Fig. 8 and Fig. S4, all the present materials show similar potential profiles of typical Mn_3O_4 phase (Fig. S4(a)) [2, 33]. The first discharge capacities of MnO_2 nanosheet, **MnAr3**, **MnAr4**, **MnAr5**, **MnAr6**, **MnAr7**, **MnAr8,** and reference Mn_3O_4 electrodes are determined as 1304, 1423, 1520, 1253, 1348, 1259, 1234, and 1437 mA g^{-1}, respectively, which are higher than the theoretical specific capacity of Mn_3O_4 (937 mAh g^{-1}). In the 1st discharge profiles of the present manganese oxide electrodes, the electrochemical redox processes occurring in the potential range of 0.3–2.0 V are attributable to a reduction from Mn_3O_4 to MnO and an irreversible process of solid electrolyte interphase (SEI) film formation. The following plateau occurring at ~ 0.3 V is assigned as a further reduction of MnO to Mn metal [2, 3, 7].

$$2Li^+ + Mn_3O_4 + 2e^- \rightarrow 3MnO + Li_2O \quad (1)$$

$$2Li^+ + MnO + 2e^- \rightarrow Mn + Li_2O \quad (2)$$

After the initial cycle, all the present materials exhibit a notable decrease of discharge capacity with proceeding the cycle, which can be ascribed to the continuous formation of SEI layers and/or to the irreversible reaction with the electrolyte [8]. In the 2nd discharge cycle, a new plateau appears at ~ 0.6 V, which is higher than that of the first discharge cycle corresponding to the formation of Li_2O and metallic Mn. After the initial several cycles, no significant capacity loss occurs for the present materials, reflecting their promising

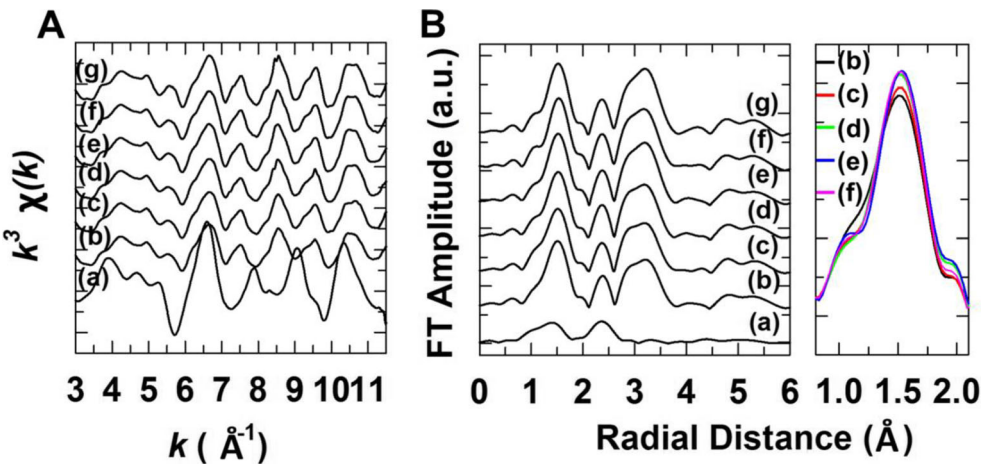

Fig. 7 (A) k^3-weighted Mn K-edge EXAFS oscillations and (B) their FT spectra of (a) the precursor MnO_2 nanosheet and its calcined derivatives of (b) **MnAr3**, (c) **MnAr4**, (d) **MnAr5**, (e) **MnAr6**, and (f) **MnAr7**, and (g) the reference Mn_3O_4

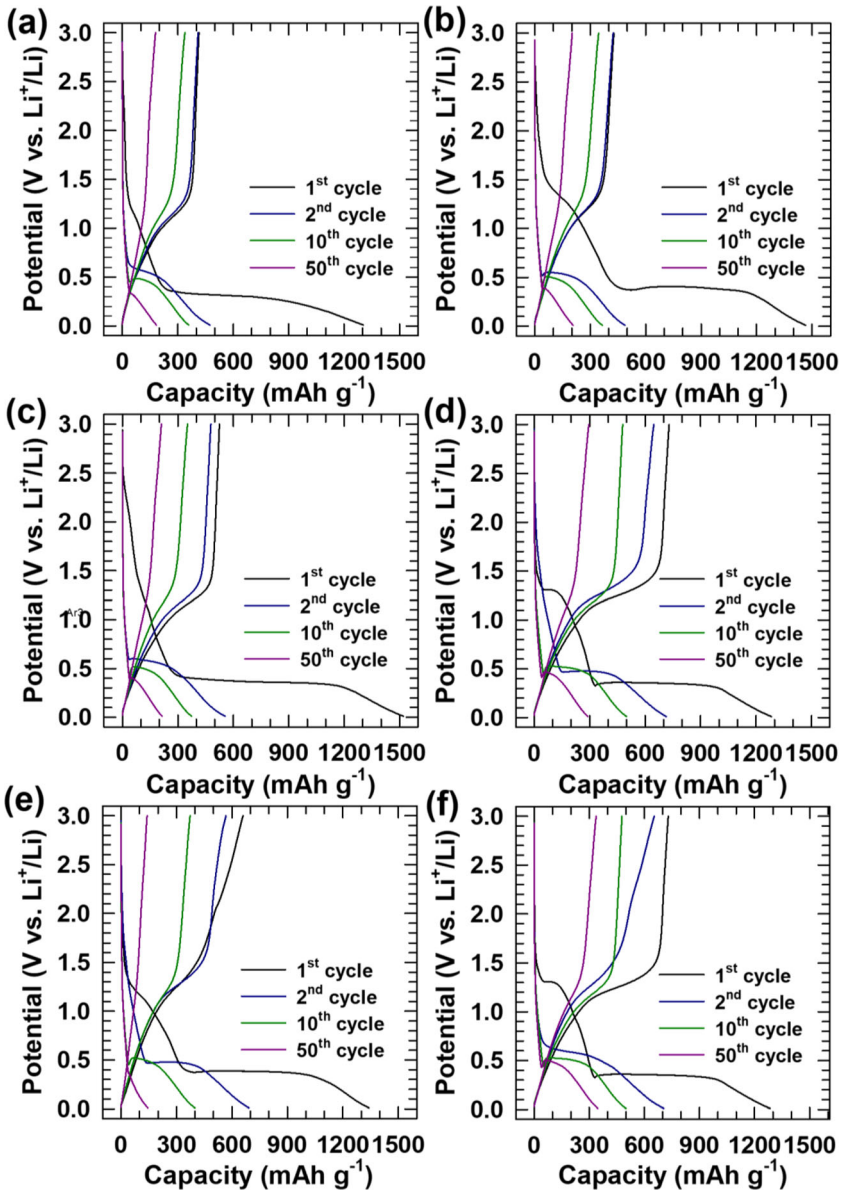

Fig. 8 Potential profiles of (a) the precursor MnO_2 nanosheet and its calcined derivatives of (b) **MnAr3**, (c) **MnAr4**, (d) **MnAr5**, (e) **MnAr6**, and (f) **MnAr7** at a current density of 100 mA g^{-1}

cyclability. Among the present materials, **MnAr7** delivers the largest discharge capacity of ~ 344 mAh g^{-1} for the 50th cycle, which is larger than those of the other materials (~ 207 mAh g^{-1} for **MnAr3**, 215 mAh g^{-1} for **MnAr4**, 290 mAh g^{-1} for **MnAr5**, 145 mAh g^{-1} for **MnAr6**, 220 mAh g^{-1} for **MnAr8**, 192 mAh g^{-1} for Mn_3O_4, and 184 mAh g^{-1} for MnO_2 nanosheet, respectively).

The electrochemical behavior of the **MnAr7** electrode is further analyzed using cyclic voltammetry (CV). As plotted in Fig. S5, the irreversible conversion reaction and the formation of SEI film occur in the potential range of 1.5–3.0 V for the 1st cycle. The cathodic peak at ~ 0.3 V corresponds to the reduction of MnO to Mn. The anodic peak at ~ 1.3 V is assigned as the conversion of Mn to MnO. After the 1st cycle, the cathodic peak corresponding to reduction from MnO to Mn is discernible at ~ 0.3 V, indicating the formation of a SEI film [34]. For the following 4 cycles, no significant changes occur in the CV profiles, confirming the good electrochemical stability of the present materials.

The rate performances of the present materials are examined by electrochemical cycling tests at several current densities, see Fig. 9B and Fig. S6. At the current densities of 100, 200, 500, and 1000 mA g^{-1}, the calcined derivatives of **MnAr5**, **MnAr6**, and **MnAr7** commonly exhibit more durable and stable rate capabilities than do the reference Mn_3O_4 crystal and the precursor MnO_2 nanosheet, highlighting the advantage of porous 2D nanosheet morphology in the electrode performance of manganese oxide especially for high current density condition. As summarized in Table S2, the present **MnAr7** material exhibits promising electrode

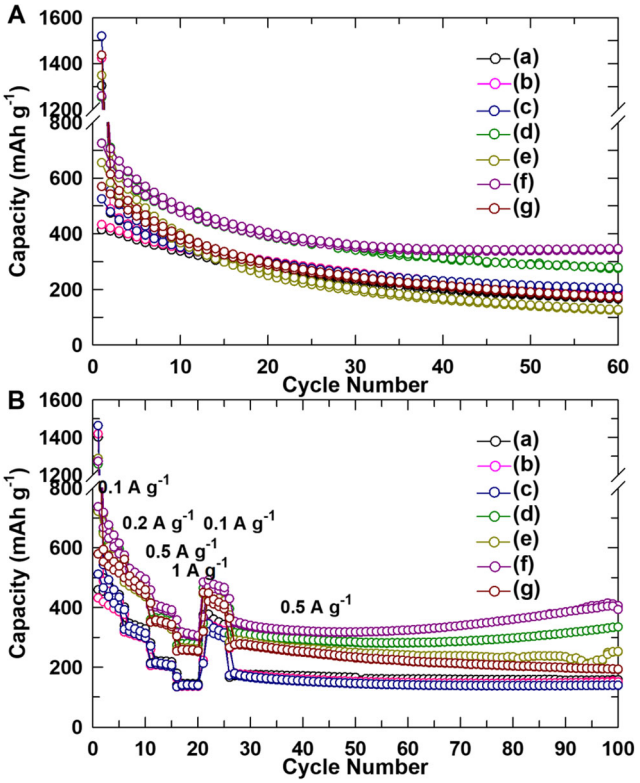

Fig. 9 (A) Capacity plots at a current density of 100 mA g^{-1} and (B) rate capability profiles at the current densities range from 100 to 1000 mA g^{-1} of (a) the precursor MnO_2 nanosheet and its calcined derivatives of (b) **MnAr3**, (c) **MnAr4**, (d) **MnAr5**, (e) **MnAr6**, and (f) **MnAr7**, and (g) the reference Mn_3O_4

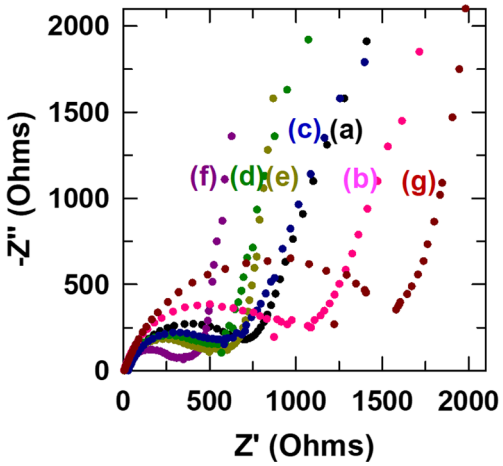

Fig. 10 Nyquist plots of (a) the precursor MnO_2 nanosheet and its calcined derivatives of (b) **MnAr3**, (c) **MnAr4**, (d) **MnAr5**, (e) **MnAr6**, and (f) **MnAr7**, and (g) the reference Mn_3O_4 over the frequency range from 100 kHz to 0.01 Hz

performance comparable with those of the other Mn_3O_4-based materials ever-reported in terms of high discharge capacity and cyclability. The observed promising electrode functionality of **MnAr7** is mainly attributable to the porous 2D nanosheet morphology, which is beneficial in improving the Li ion storage and ion diffusion ability. As found from the powder XRD results, the **MnAr7** material displays the presence of small amount of impurity Mn_2O_3 and MnO_2 phases as well as major Mn_3O_4 phase, which can make additional contribution to the improved electrode performance of this material. Actually, it is well-documented that the co-existence of mixed metal oxide phases with different valance states/polymorphs has beneficial effect on the electrode performance of Li ion batteries [8, 33, 35–38]. It is worthwhile to mention that, at 0.5 A g^{-1}, the **MnAr7** material exhibits a gradual increase of discharge after the 50th cycle capacity as well as initial capacity fading. The observed non-monotonous variation of discharge capacity is attributable to the following factors. A highly 2D porous morphology of **MnAr7** material leads to the improvement of charge and ion diffusion paths during the extended electrochemical cycling. The intimate interfacial contact between **MnAr7** electrode and electrolyte enhances the formation of polymer/gel-like film by kinetically activated electrolyte degradation, which is beneficial in the improvement of electrode functionality [39–42]. As found from FE-SEM and TEM results, the **MnAr7** electrode material shows loosely ordered porous 2D assembly of Mn_3O_4 nanocrystals, which is quite effective in maintaining nanocrystalline nature of electrode material during the extended electrochemical cyclings via the depressed agglomeration of electrode particles. Such a maintenance of nanocrystallinity has beneficial effect on the discharge capacity of calcined derivatives, as reported for many metal oxide–based anode materials [13, 16, 22, 43–45].

The evolution of charge transfer kinetics upon the heat treatment is examined with EIS analysis. Figure 10 presents the Nyquist plots of the porous 2D Mn_3O_4 nanosheets as well as Mn_3O_4 crystal and MnO_2 nanosheet. All the present materials display the semicircle at high-to-medium frequencies reflecting charge transfer resistance at the electrode/electrolyte interface [22, 33]. The diameter of this semicircle is smaller for the porous Mn_3O_4 nanosheets than that for the reference Mn_3O_4 crystal and the pristine MnO_2 nanosheet, confirming the enhancement of charge transfer kinetics and lithium ion diffusivity due to the formation of open porous 2D nanosheet. Such improved charge and ion transports are mainly responsible for the excellent electrode performance of porous Mn_3O_4 nanosheet.

4 Conclusion

In this study, porous 2D nanosheets of low-valent Mn_3O_4 material were synthesized by a thermally induced phase transition of the precursor MnO_2 nanosheet at elevated temperature. The resulting porous 2D Mn_3O_4 nanosheets demonstrate promising LIB electrode performance with large discharge capacities and promising rate capabilities and cyclabilities.

The improved electrode functionality of porous Mn_3O_4 nanosheet can be ascribed to the enhancement of charge and ion diffusion and the maintenance of nanocrystalline nature during the electrochemical cycling. Taking into account the redoxable nature and catalytic activity of low-valent manganese oxides [4, 46–48], the present porous 2D Mn_3O_4 nanosheet is also supposed to show promising functionalities as electrocatalysts and redox catalysts. Since the present phase transformation route is applicable for other redoxable transition metal oxide nanosheet, our current project is to synthesize various porous 2D nanosheets of transition metal oxides such as cobalt oxide, nickel oxide, and vanadium oxide and to employ the resulting materials for electrodes and electrocatalysts.

Funding information This work was supported by the National Research Foundation of Korea (NRF) grant funded by the Korea government (MSIP) (No. NRF-2017R1A2A1A17069463) and by the Korea government (MSIT) (No. NRF-2017R1A5A1015365). The experiments at PAL were supported in part by MOST and POSTECH.

Compliance with ethical standards

Conflict of interest The authors declare that they have no conflict of interest.

References

1. S.M. Oh, S.B. Patil, X. Jin, S.-J. Hwang, Chem. Eur. J. **24**, 4757 (2018)
2. J. Yue, X. Gu, L. Chen, N. Wang, X. Jiang, H. Xu, J. Yang, Y. Qian, J. Mater. Chem. A **2**, 17421 (2014)
3. J. Wang, X. He, E. Paillard, N. Laszczynski, J. Li, S. Passerini, Adv. Energy Mater. **6**, 1600906 (2016)
4. X. Jin, J. Lim, Y. Ha, N.H. Kwon, H. Shin, I.Y. Kim, N.-S. Lee, M.H. Kim, H. Kim, S.-J. Hwang, Nanoscale **9**, 12416 (2017)
5. D. Gao, S. Luo, Y. Zhang, J. Liu, H. Wu, S. Wang, P. He, J. Solid State Electrochem. **22**, 3409 (2018)
6. R. Wang, X. Li, Z. Wang, H. Guo, J. Solid State Electrochem. **20**, 19 (2016)
7. X. Gu, J. Yue, L. Li, H. Xue, J. Yang, X. Zhao, Electrochim. Acta **184**, 250 (2015)
8. X. Jiang, Y. Wang, L. Yang, D. Li, H. Xu, Y. Ding, J. Power Sources **274**, 862 (2015)
9. M. Manickam, P. Singh, T.B. Issa, S. Thurgate, R. De Marco, J. Power Sources **130**, 254 (2004)
10. X. Fang, X. Lu, X. Guo, Y. Mao, Y.-S. Hu, J. Wang, Z. Wang, F. Wu, H. Liu, L. Chen, Electrochem. Commun. **12**, 1520 (2010)
11. F. Jiao, P.G. Bruce, Adv. Mater. **19**, 657 (2007)
12. J.-Y. Luo, J.-J. Zhang, Y.-Y. Xia, Chem. Mater. **18**, 5618 (2006)
13. H. Lai, J. Li, Z. Chen, Z. Huang, ACS Appl. Mater. Interfaces **4**, 19 (2012)
14. C. Tan, X. Cao, X.-J. Wu, Q. He, J. Yang, X. Zhang, J. Chen, W. Zhao, S. Han, G.-H. Nam, M. Sindoro, H. Zhang, Chem. Rev. **117**, 6225 (2017)
15. L. Sheng, S. Liang, T. Wer, J. Chang, Z. Jiang, L. Zhang, Q. Zhou, J. Zhou, L. Jiang, Z. Fan, Energy Storage Mater. **12**, 94 (2018)
16. M. Zhen, Z. Zhang, Q. Ren, L. Liu, Mater. Lett. **177**, 21 (2016)
17. Y. Omomo, T. Sasaki, L. Wang, M. Watanabe, J. Am. Chem. Soc. **125**, 3568 (2003)
18. K. Kai, Y. Yoshida, H. Kageyama, G. Saito, T. Ishigaki, Y. Furukawa, J. Kawamata, J. Am. Chem. Soc. **130**, 15938 (2008)
19. K. Adpakpang, S.M. Oh, D.A. Agyeman, X. Jin, N. Jarulertwathana, I.Y. Kim, T. Sarakonsri, Y.-M. Kang, S.-J. Hwang, Adv. Funct. Mater. **28**, 1707106 (2018)
20. L. Li, G. Jiang, R. Sun, B. Cao, New J. Chem. **41**, 15283 (2017)
21. R. Jia, J. Yue, Q. Xia, J. Xu, X. Zhu, S. Sun, T. Zhai, H. Xia, Energy Storage Mater. **13**, 303 (2018)
22. Y.-C. Zhang, J.-T. Li, Z.-G. Wu, L. Huang, S.-G. Sun, J. Alloys Compd. **721**, 229 (2017)
23. S.-Z. Huang, J. Jin, Y. Cai, Y. Li, H.-Y. Tan, H.-E. Wang, G.V. Tendeloo, B.-L. Su, Nanoscale **6**, 6819 (2014)
24. Y. Wang, S. Niu, S. Lu, Mater. Lett. **158**, 416 (2015)
25. C. Chen, G. Ding, D. Zhang, Z. Jiao, M. Wu, C.-H. Shek, C.M.L. Wu, J.K.L. Lai, Z. Chen, Nanoscale **4**, 2590 (2012)
26. S. J. Gregg, K. S. W. Sing (eds.), *Adsorption, Surface Area and Porosity*, 2nd edn. (Academic Press Inc., LONDON, 1982)
27. S.-J. Hwang, H.-S. Park, J.-H. Choy, G. Campet, Chem. Mater. **12**, 1818 (2000)
28. S.-J. Hwang, C.-W. Kwon, J. Portier, G. Campet, H.-S. Park, J.-H. Choy, P.V. Huong, M. Yoshimura, M. Kakihana, J. Phys. Chem. B **106**, 4053 (2002)
29. A.-N.I. Gonsmov, V.A. Dnrrs, Am. Mineral. **77**, 33 (1992)
30. I. Zaharieva, M.M. Najafpour, M. Wiechen, M. Haumann, P. Kurz, H. Dau, Energy Environ. Sci. **4**, 2400 (2011)
31. D. Shevchenko, M.F. Anderlund, S. Styring, H. Dau, I. Zaharieva, A. Thapper, Phys. Chem. Chem. Phys. **16**, 11965 (2014)
32. Y. Gorlin, B. Lassalle-Kaiser, J.D. Benck, S. Gul, S.M. Webb, V.K. Yachandra, J. Yano, T.F. Jaramillo, J. Am. Chem. Soc. **135**, 8525 (2013)
33. K. Adpakpang, X. Jin, S. Lee, S.M. Oh, N.-S. Lee, S.-J. Hwang, ACS Appl. Mater. Interfaces **8**, 13360 (2016)
34. N. Palaniyandy, F.P. Nkosi, K. Raju, K.I. Ozoemena, J. Electroanal. Chem. **833**, 79 (2019)
35. R. Li, C. Lin, N. Wang, L. Luo, Y. Chen, J. Li, Z. Guo, Adv. Comps. Hybrid Mater. **1**, 440 (2018)
36. S.B. Patil, I.Y. Kim, J.L. Gunjakar, S.M. Oh, T. Eom, H. Kim, S.-J. Hwang, ACS Appl. Mater. Interfaces **7**, 18679 (2015)
37. S. Wang, Y. Yang, W. Quan, Y. Hong, Z. Zhang, Z. Tang, J. Li, Nano Energy **32**, 294 (2017)
38. Y. Liu, L. Lin, W. Zhang, M. Wei, Sci. Rep. **7**, 1 (2017)
39. W. Dang, F. Wang, Y. Ding, J. Alloys Compd. **690**, 72 (2017)
40. W. Dang, W. Wang, Y. Yang, Y. Wang, J. Huang, X. Fang, L. Wu, Z. Rong, X. Chen, X. Li, L. Huang, X. Tang, Electrochim. Acta **313**(99) (2019)
41. J.-S. Do, C.H. Weng, J. Power Sources **146**, 482 (2005)
42. X. Li, L. Qiao, D. Li, X. Wang, W. Xie, D. He, J. Mater. Chem. A **1**, 6400 (2013)
43. I.Y. Kim, S.H. Lee, H.-W. Ha, T.W. Kim, Y.S. Han, J.K. Kang, D.H. Lee, S.-J. Hwang, J. Power Sources **195**, 6101 (2010)
44. S.M. Oh, I.Y. Kim, K. Adpakpang, S.-J. Hwang, Electrochim. Acta **174**, 391 (2015)
45. H.B. Wu, J.S. Chen, H.H. Hong, X.W. Lou, Nanoscale **4**, 2526 (2012)
46. D.M. Robinson, Y.B. Go, M. Greenblatt, G.C. Dismukes, J. Am. Chem. Soc. **132**, 11467 (2010)
47. A. Indra, P.W. Menezes, I. Zaharieva, E. Baktash, J. Pfrommer, M. Schwarze, H. Dau, M. Driess, Angew. Chem. Int. Ed. **52**, 13206 (2013)
48. T. Takashima, K. Hashimoto, R. Nakamura, J. Am. Chem. Soc. **134**, 18153 (2012)